The Doppler Aerosol Wind (DAWN) Airborne, Wind-Profiling Coherent-Detection Lidar System: Overview and Preliminary Flight Results

MICHAEL J. KAVAYA, JEFFREY Y. BEYON, GRADY J. KOCH, MULUGETA PETROS,
PAUL J. PETZAR, UPENDRA N. SINGH, BO C. TRIEU, AND JIRONG YU

NASA Langley Research Center, Hampton, Virginia

ABSTRACT

The first airborne wind measurements of a pulsed, 2-μm solid-state, high-energy, wind-profiling lidar system for airborne measurements are presented. The laser pulse energy is the highest to date in an eye-safe airborne wind lidar system. This energy, the 10-Hz laser pulse rate, the 15-cm receiver diameter, and dual-balanced coherent detection together have the potential to provide much-improved lidar sensitivity to low aerosol backscatter levels compared to earlier airborne-pulsed coherent lidar wind systems. Problems with a laser-burned telescope secondary mirror prevented a full demonstration of the lidar's capability, but the hardware, algorithms, and software were nevertheless all validated. A lidar description, relevant theory, and preliminary results of flight measurements are presented.

1. Introduction

a. Background

The primary motivation for wind measurement technology development at the National Aeronautics and Space Administration (NASA) is to prepare for an Earth-orbiting lidar system to globally measure vertical profiles of horizontal wind magnitude and direction (horizontal vector winds). This mission is one of 15 earth science missions recommended to NASA by the National Research Council (NRC), which they call "3D Winds" (NRC 2007). Required preparation for this space mission includes formulation of the wind measurement requirements, technology development and validation, measurement technique development and validation, atmospheric characterization, theoretical advancement, computer simulation of measurement performance advancement, and ground and airborne measurement demonstration. Computer simulations began over three decades ago [Huffaker et al. 1984; atmospheric characterization has been advanced, especially for global aerosol backscatter levels (Menzies and Tratt 1997); relevant theory has been developed by many groups; mission overviews have been published (Baker et al. 1995; Singh et al. 2005); and the measurement requirements have been developed (NASA 2006)]. Here we report on the first aircraft flights of a pulsed, 2-μm, coherent-detection lidar system having basic laser parameters matching those required for a space mission. Because of the advanced laser, the lidar system can provide the best sensitivity to aerosol backscatter levels to date for this type of airborne wind lidar.

b. Lidar system

A block diagram of the Doppler Aerosol Wind (DAWN) lidar system is shown in Fig. 1. The pulsed solid-state laser uses the Ho:Tm:LuLiF lasing crystal with laser diode array (LDA) side pumping. The pulsed laser resonator closely follows the wavelength of the injected seed laser. The laser emits nominally 250-mJ pulses at a 10-Hz rate. The linearly polarized laser pulse is converted to circular polarization by a transmit–receive switch comprising a polarizing beam splitter and a quarter-wave plate. The 15-cm beam-expanding telescope expands the input pulse to approximately the optimum 12-cm diameter (Rye and Frehlich 1992). The expanded beam is directed to nadir and enters an optical wedge that deflects the pulse by 30.12°. The azimuthal direction of the wedge's deflection is chosen by a computer-controlled ring motor that can turn the optical wedge about a nominal nadir axis. As the pulse

Corresponding author address: Michael J. Kavaya, NASA Langley Research Center, 5 N. Dryden St., Mail Code 468, Hampton, VA 23681.
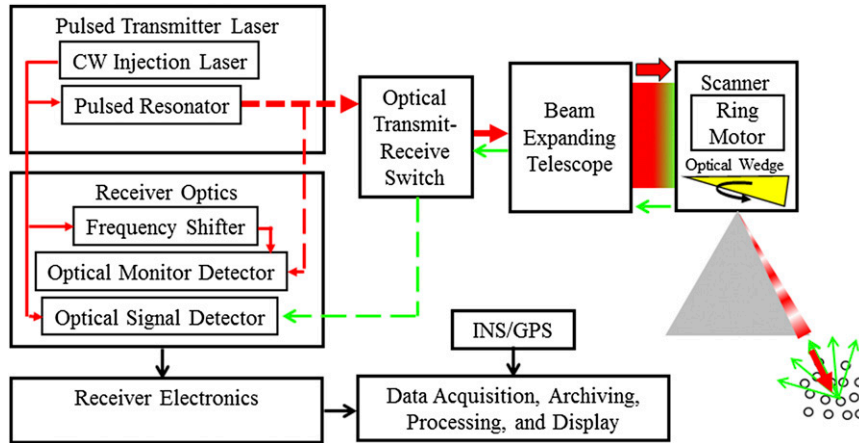E-mail: michael.j.kavaya@nasa.gov

FIG. 1. Block diagram of the DAWN lidar system.

travels away from the airplane, the aerosol and cloud particles it intercepts scatter the light in many directions, including a small fraction directed back (backscattered) to the lidar system. The backscattered light as measured from the moving aircraft is Doppler frequency shifted by an amount proportional to the projection of the airplane and wind velocity into the direction of the pulse. The backscattered light, which reenters the lidar system, is directed to the optical signal detector, where it is heterodyned or mixed with a portion of the injection laser. The injection laser also serves the role of a local oscillator (LO) laser. Part of the transmitted pulse is directed to an optical monitor detector where it is mixed with a frequency upshifted portion of the injection laser. The frequency shifter, an acousto-optic modulator (AOM), permits determination of the magnitude and sign of the frequency different between the injection laser and the pulsed laser. Knowing this frequency difference, the projected aircraft velocity, and the AOM frequency, permits calculation of the projected wind velocity. When this is repeated for several scanner azimuth angles, the three components of the wind velocity may be determined. Major lidar system subsystems not shown in Fig. 1 include power supplies, control circuits, laser cooling equipment, rigid mechanical structure for inter-component alignment stability, processing algorithms, and software. Many more details about the lidar system will be given in section 3.

The rest of this paper will describe the theory used for geometry, Doppler shift, coordinate system conversions, alignment error compensation, and signal processing; provide more details on the Doppler lidar system; and present preliminary flight measurement results from NASA's hurricane Genesis and Rapid Intensification Processes (GRIP) aircraft campaign in 2010.

2. Theory

a. Geometry

Our wind-measurement flight geometry is depicted in Fig. 2, using the right-handed Cartesian geographic northeast-down (NED) coordinate system. Consider any vector $\mathbf{V}$. In NED, the polar angle θ goes from the positive geographic down (z) axis to the three-dimensional (3D) vector. The azimuth angle ϕ lies in the north–east (x–y) horizontal plane, and goes from the positive geographic north (x) axis, moving toward (and possibly past) the positive east (y) axis, to the projection of the 3D vector into the north–east plane. The lidar-carrying aircraft is flying approximately level, with the 3D aircraft nose (body forward) direction vector $\mathbf{F}_A$ (unitless) and the 3D aircraft velocity vector $\mathbf{V}_A$ (m s^{-1}). The projections of these vectors into the horizontal plane are vectors $\mathbf{F}_{AH}$ and $\mathbf{V}_{AH}$, where the subscript AH stands for "aircraft horizontal". In aviation, $\mathbf{F}_{AH}$ defines the aircraft heading angle $\phi_{\mathbf{F}}$ (rad) and $\mathbf{V}_{AH}$ defines the aircraft track angle $\phi_{\mathbf{V}}$ (rad). The angle $\phi_{\mathbf{VF}} = \phi_{\mathbf{V}} - \phi_{\mathbf{F}}$ (rad) is the aircraft drift angle caused by horizontal crosswinds. For the crosswind blowing primarily toward the east (westerly wind, Fig. 2) or west (easterly wind), either $\mathbf{F}_{AH}$ or $\mathbf{V}_{AH}$ may be closer to geographic north, meaning the drift angle is positive or negative, respectively. The wind, carrying natural aerosol particles along at the same velocity, has 3D velocity vector $\mathbf{V}_W$ (m s^{-1}) and horizontal projection $\mathbf{V}_{WH}$; $\mathbf{V}_{WH}$ has azimuth angle ϕ_W (rad).

During wind measurements, the airborne lidar sets the lidar scanner azimuth angle ϕ_S (rad) and then fires several laser pulses with 3D velocity vector $c\mathbf{I}_L$ (m s^{-1}; or possibly unequal vectors $c\mathbf{I}_{L,i}$ for each pulse i), where $\mathbf{I}_L$ is a unit length vector in the laser pulse direction and c (m s^{-1}) is the speed of light; $\mathbf{I}_{LH}$ and ϕ_L are not shown
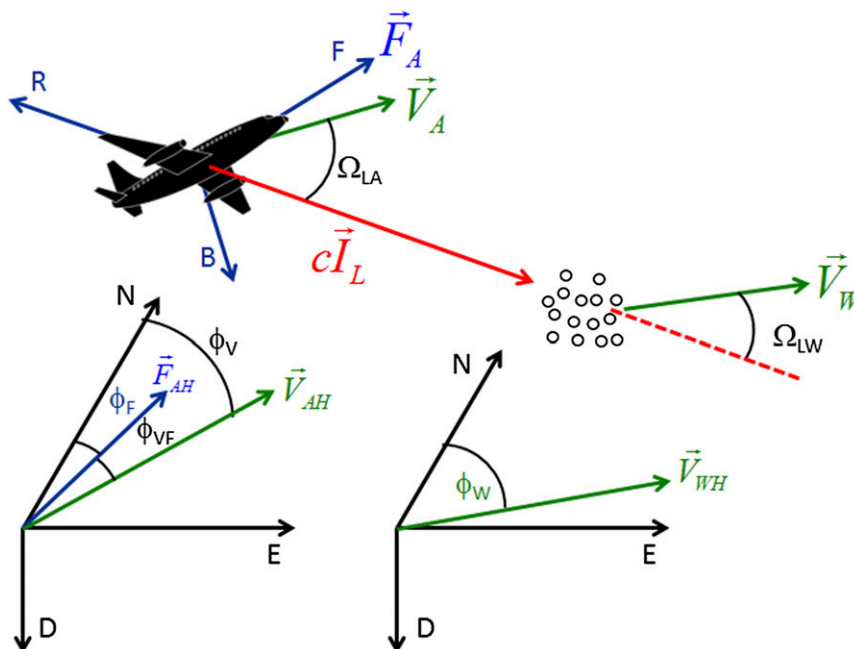
FIG. 2. Geometry for the airborne lidar measurement of wind.

in Fig. 2. The illuminated aerosol particles backscatter a small fraction of the laser pulse's energy along 3D direction vector $c\mathbf{I}_L$ and into the lidar system's receiver for detection. In our case, as is typical for coherent lidar, the transmit telescope is also the receive telescope. Because of special relativity, translation of the airplane does not cause any transmit–receive phase front misalignment (misalignment of the received phase front with respect to the transmitted phase front; Gudimetla and Kavaya 1999). Airplane rotations do cause misalignment. The laser velocity vector $c\mathbf{I}_L$ makes 3D angles Ω_{LA} and Ω_{LW} (rad) with $\mathbf{V}_A$ and $\mathbf{V}_W$, respectively.

The airplane has a conceptual, right-handed, forward-right-belly (FRB) coordinate system attached to its airframe. This coordinate system is used in two ways. First, the lidar scanner is mounted and calibrated with the goal that its setting provides the transmitted laser beam direction relative to the FRB coordinates. Second, the lidar system's inertial navigation system–global positioning system (INS–GPS), which is mounted to the lidar (see Fig. 1), provides the yaw, pitch, and roll angles of the physical case of the INS–GPS with respect to the NED coordinate axes. The goal is that these three angles also represent the rotations of the FRB axes (airplane body) with respect to the NED coordinate axes. In practice, neither of these goals is perfectly met, and extra calibration steps are required.

Both the transmitted laser pulse and the backscattered light travel at approximately the vacuum speed of light $c = 299\,792\,458$ (m s^{-1}). We model the transmitted laser

pulse power temporal shape with a 1D Gaussian function truncated at ± 3 standard deviations, where it is about 1.1% of the center height. For the Gaussian shape, the pulse will reach 50% of its center height at $-(2\ln 2)^{0.5} = -1.1774$ standard deviations; and we arbitrarily let $t = 0$ (s) be at this point in the pulse. The pulse duration is defined as the full width at half maximum (FWHM), and has duration t_L (s) = 2.355 standard deviations. The pulse rate is frequency f_L (Hz).

The lidar receiver's signal at time t is primarily due to all the aerosol particles illuminated by the laser pulse and positioned between minimum range $c(t - t_L)/2$ and maximum range $ct/2$ (Kavaya and Menzies 1985). Range is proportional to time. The best or smallest possible range resolution is approximately the length of this range interval, which is $R_{\mathrm{RES,MIN}} \sim ct_L/2$. The transmitted laser pulse intensity spatial cross section typically has a shape similar to the modeled temporal shape, except the Gaussian is 2D with a spatial standard deviation different from the temporal standard deviation. It is useful to conceptually think of a circular cross section that includes 86.5% of the intensity. This circle extends to the radius that has $e^{-2} = 13.5\%$ of the on-axis intensity (i.e., extends radially to two spatial standard deviations from center). In general, combined with the temporal shape, this "cylindrically" shaped volume of air may contain different values of laser pulse power, laser pulse frequency (chirp), aerosol concentrations, wind velocity, and wind turbulence. For our DAWN lidar system, typical values are $t_L \sim 180$ ns and $R_{\mathrm{RES,MIN}} \sim ct_L/2 \sim 27$ m.

In operation, the lidar receiver detector signal is digitized by an analog-to-digital converter (ADC) at sampling rate $f_{ADC} = 1/T_{ADC}$ (sample s^{-1} or Hz), so that further signal processing may be performed by a computer. This is easier and has more options than performing signal processing with optical or analog electronic components. The continuous string of ADC signal samples from each laser shot is grouped into sets of N_{RG} (sample) consecutive signal samples, which are called range gates (RG). Successive range gates provide a range profile of the wind. The range gate observation time is $T_{RG} = N_{RG}/f_{ADC}$ (s), and the range resolution (m) of a range gate is $R_{RG} \sim (c/2)(t_L + N_{RG}/f_{ADC})$. DAWN typical values are $f_{ADC} = 500 \times 10^6$ samples per second (10^6 samples = 1 Msample), $T_{ADC} = 2$ ns, $N_{RG} = 512$, $N_{RG}/f_{ADC} \sim 1.02 \mu$s, and $R_{RG} \sim 180.5$ m.

b. Doppler shift equation

The coherent-detection Doppler lidar system is designed to measure the change in light frequency between the transmitted laser pulse and the backscattered (received) light. Referring to Fig. 2, the equation linking the light frequency change, the velocities, and the angles is (Taff 1983)

$$(\nu_R - \nu_L) = \nu_L \frac{2\beta_A \cos\Omega_{AL} - 2\beta_W \cos\Omega_{LW}}{(1 + \beta_W \cos\Omega_{LW})(1 - \beta_A \cos\Omega_{AL})}, \quad (1)$$

$$\beta_A = \frac{|\mathbf{V}_A|}{c} \quad \text{and} \quad \beta_W = \frac{|\mathbf{V}_W|}{c}. \quad (2)$$

We use ν to indicate very high-optical frequencies as opposed to the English letter f for lower frequencies, subscript L to indicate the laser's transmitted frequency, subscript R to indicate the backscattered received optical frequency, subscript A for the aircraft, and subscript W for the wind. Equations (1) and (2) include special relativity and are valid for any airplane (lidar platform) and wind velocities. Equation (1) has never been published in a widely available journal to our knowledge, and so we include it here. For the airplane flights described herein, we may use the limit of small velocities compared to light speed. Both terms in Eq. (2) approach 0, and Eq. (1) becomes

$$(\nu_R - \nu_L) \approx \nu_L (2\beta_A \cos\Omega_{AL} - 2\beta_W \cos\Omega_{LW}). \quad (3)$$

(The tangential velocity of a spacecraft will be much larger than an aircraft's velocity. A recent investigation showed the approximation in (3) could lead to a wind velocity error of about 0.1 m s^{-1} (Ashby 2007), which is probably too large to ignore with overall wind error goals of 1–3 m s^{-1} from all contributions.

We next combine Eqs. (2) and (3), use the vector dot product expressions,

$$\cos\Omega_{AL} = \frac{\mathbf{V}_A \cdot (c\mathbf{I}_L)}{[|\mathbf{V}_A||(c\mathbf{I}_L)|]} \quad \text{and} \quad \cos\Omega_{LW} = \frac{c\mathbf{I}_L \cdot \mathbf{V}_W}{[|(c\mathbf{I}_L)||\mathbf{V}_W|]}, \quad (4)$$

and use the spherical coordinate system definitions for the polar θ_L and azimuth ϕ_L angles (rad),

$$I_{LX} = \sin\theta_L \cos\phi_L, \quad I_{LY} = \sin\theta_L \sin\phi_L,$$
$$I_{LZ} = \cos\theta_L, \quad \text{and} \quad \theta_L : 0° - 180°, \quad \phi_L : 0° - 360°, \quad (5)$$

to obtain

$$(\nu_R^i - \nu_L^i) = \frac{2}{\lambda_L} [\sin\theta_L^i \cos\varphi_L^i (V_{AX}^i - V_{WX})$$
$$+ \sin\theta_L^i \sin\varphi_L^i (V_{AY}^i - V_{WY})$$
$$+ \cos\theta_L^i (V_{AZ}^i - V_{WZ})], \quad (6)$$

where $\lambda_L = c/\nu_L$ (m) is the transmitted laser pulse wavelength and x, y, and z represent any arbitrary right-handed coordinate reference frame. In practice the user must select the coordinate system in which to use Eq. (6)—see section 2c below for a discussion of different coordinate systems. A superscript i has been added to variables expected to change with different lidar scanner azimuth angles ϕ_L. The reason that the superscript is on the laser beam polar angle θ_L is to allow the possibility that changes in azimuth angle ϕ_L cause changes in the polar angle. The three wind velocity components are assumed to be constant for all azimuth angles in a scan pattern.

All possible directions of the transmitted laser beam have a unique pair of angles (θ_L, ϕ_L)—these angles with subscript L represent the *actual direction of the laser beam outside the airplane* and are not necessarily equal to the *settings of the lidar scanner* (θ_S, ϕ_S)—because imperfections in the lidar scanner, lidar assembly and alignment, and lidar mounting to the aircraft frame may introduce angle changes. These angle changes may not be simple angle offsets but may be functional, $(\theta_L, \phi_L) = f(\theta_S, \phi_S)$; that is, changes in the lidar scanner azimuth angle may change the laser beam polar angle. For the flights reported here, scanner setting values were approximately $\theta_S = 30.12°$, and $\phi_S = -45°, -22.5°, 0°, 22.5°,$ and $45°$. The five azimuth angles comprised a scan pattern.

The unknown quantities in Eq. (6) are the three components of the wind velocity vector $\mathbf{V}_W$. Therefore, for

wind data processing, at least three copies of Eq. (6) with different values of the lidar scanner azimuth angle ϕ_S must be simultaneously solved for the wind components. If we assume the vertical wind $V_{WZ} = 0$, then at least two copies of Eq. (6) are needed.

We initially solved the data processing algorithm using only two azimuth angles and equations, and assumed vertical wind = 0. We used $\phi_S = -45°$ and $45°$, and did not use the recorded data from the other three azimuth angles. Later we solved the data processing algorithm using all five azimuth angles and were able to calculate vertical wind also.

c. Using four different coordinate systems

The angles and velocities in Eq. (6) must all be referenced to the same coordinate system. Then the solution from Eq. (6) must be converted to the coordinate system desired by the meteorological wind user community. We had to deal with four coordinate systems:

1) The FRB coordinates of the airplane. The laser beam direction outside the airplane is known with respect to FRB using the lidar scanner settings and the angle-converting functional equation.
2) The NED coordinates. Our lidar-mounted INS–GPS unit provided yaw, pitch, and roll angles of the airplane body in NED. INS–GPS roll and pitch errors are specified as 1.0 mrad–1σ. Heading error = yaw error is specified as 1.5 mrad and up, depending on the recent aircraft horizontal accelerations. When all three aircraft rotations equal zero, the FRB axes are aligned with the NED axes. (Heading equals yaw because we are dealing with an airplane and the aviation word for *yaw* in NED is *heading*.)
   If the horizontal wind direction (HWD) is plotted as arrows in a top-view plot, then the meteorological community wants the arrow to point in the direction of the air movement. This indicates the NED system. For example, if air is blowing east, then the NED azimuth angle is 90°. The community wants the arrow to point with a heading of 90° in the plot.
3) The east–north–up (ENU) coordinates. Our INS–GPS unit provided the three components of the aircraft velocity in ENU. The velocity component errors are all specified as 0.1 m s^{-1}–1σ. The meteorological community prefers the vertical wind to be labeled positive if the air is moving up, which indicates the ENU system.
4) The southwest-down (SWD) coordinates. If the horizontal wind is reported with a numerical azimuth angle, then the meteorological community prefers the direction from which the air is coming. This indicates

the SWD system. For example, if air is blowing east like in the NED discussion, then the SWD azimuth angle is 270°. Reporting the number 270° in NED means the direction west. The meteorological community calls the wind a westerly wind and will interpret the 270° in NED correctly.

One processing option is to use Eq. (6) entirely in the ENU coordinate system. The laser frequency difference and wavelength do not change with the coordinate system. The aircraft velocity components V_A are already provided in ENU. The lidar scanner settings and functional equation provide the laser beam direction with respect to FRB, which is also with respect to NED before aircraft rotations. The laser direction vector outside the aircraft is then rotated within NED by applying the appropriate rotation matrices using the aircraft body rotations. (The next section describes the rotation matrices.) Further conversion of the laser direction vector to ENU is straightforward. Several copies of Eq. (6) are then used to solve for the three components of wind velocity in ENU. The vertical wind component is reported in ENU. The horizontal wind direction is reported either in NED or SWD as discussed above.

d. 3D rotation matrix due to roll, pitch, and yaw in NED

As stated above, a key step before using Eq. (6) is to rotate the laser beam direction outside the airplane using the aircraft rotation angles provided by the INS–GPS unit and staying in the NED system. We begin with the three Cartesian 3D rotation matrices (Goldstein et al. 2001, section 4.2):

$$\mathbf{R}_X = \begin{bmatrix} 1 & 0 & 0 \\ 0 & \cos\Psi_X & -\sin\Psi_X \\ 0 & \sin\Psi_X & \cos\Psi_X \end{bmatrix}$$

$$\mathbf{P}_Y = \begin{bmatrix} \cos\Psi_Y & 0 & \sin\Psi_Y \\ 0 & 1 & 0 \\ -\sin\Psi_Y & 0 & \cos\Psi_Y \end{bmatrix}$$

$$\mathbf{Y}_Z = \begin{bmatrix} \cos\Psi_Z & -\sin\Psi_Z & 0 \\ \sin\Psi_Z & \cos\Psi_Z & 0 \\ 0 & 0 & 1 \end{bmatrix}. \tag{7}$$

These matrices represent, from top to bottom roll ($\mathbf{R}$) about the x axis by angle Ψ_X (rad), pitch ($\mathbf{P}$) about the y axis by Ψ_Y, and yaw ($\mathbf{Y}$) about the z axis by Ψ_Z. The capital

roman letter indicates the popular name of the rotation, while the subscript indicates the axis of rotation. The matrix element indices with negative signs are 23, 31, and 12, respectively. Defining the number sequence 123123, the indices with negative signs all follow the sequence order. These matrices *rotate a vector direction while holding the coordinate axes constant in inertial space*, giving the three new vector components of the rotated vector in the original coordinate system. For the inverse matrices of the three rotation matrices, which are their transposes since they are orthogonal matrices, the indices of the negative components would be 32, 13, and 21, respectively. They are in the reverse order of the 123123 sequence. They would *rotate the coordinate axes while holding the vector direction constant in inertial space*, giving the three vector components of the original vector in the new rotated coordinate system.

Our particular INS–GPS unit [Systron Donner Inertial C–Miniature Integrated GPS/INS Tactical System (MIGITS) III] assumes that 1) the rotation order is yaw, then pitch, then roll; 2) the rotation angles it provides will be used in rotation matrices that rotate the coordinate axes; and 3) all rotations are counterclockwise (CCW) when looking down the rotation axis from infinity. (Caution is advised since these assumptions may differ with different INS–GPS units.) Because of the second assumption by the INS–GPS, we must use the inverse matrices of those in Eq. (7) to match the INS–GPS. The result of doing that will be an overall 3D rotation of the coordinate axes. But we need to rotate the laser beam vector and not the coordinate axes, so one final inverse of the total is needed. To properly combine the rotation matrices in Eq. (7) to rotate the laser beam vector, we must use the following rotation equation:

$$
\begin{bmatrix} I_{LX}^{ROT} \\ I_{LY}^{ROT} \\ I_{LZ}^{ROT} \end{bmatrix} = (M) \begin{bmatrix} I_{LX} \\ I_{LY} \\ I_{LZ} \end{bmatrix} = [(\mathbf{R}_X^{-1})(\mathbf{P}_Y^{-1})(\mathbf{Y}_Z^{-1})]^{-1} \begin{bmatrix} I_{LX} \\ I_{LY} \\ I_{LZ} \end{bmatrix} = (\mathbf{Y}_Z)(\mathbf{P}_Y)(\mathbf{R}_X) \begin{bmatrix} I_{LX} \\ I_{LY} \\ I_{LZ} \end{bmatrix}.
\tag{8}
$$

e. Finding the functional equation and its parameters

Before processing the wind data, it is necessary to find the parameter values of the mounting and alignment imperfection functional equation that converts the lidar

scanner settings to the actual direction of the laser beam outside the aircraft. This equation is found by modeling the possible mounting and optical alignment imperfections. Without showing the lengthy derivation, an example of a functional equation for DAWN is

$$
A_4 = \phi_S + A_3,
$$
$$
\theta_L = \cos^{-1}[-\sin\theta_S \sin A_1 \cos(A_4 - A_2) + \cos\theta_S(\cos A_1)],
$$
$$
\phi_L = \tan^{-1}\left\{ \frac{[-\sin\theta_S \cos A_4 \sin A_2 \cos A_2(1 - \cos A_1) + \sin\theta_S \sin A_4(\cos A_1 \sin^2 A_2 + \cos^2 A_2) + \cos\theta_S(\sin A_2 \sin A_1)]}{[\sin\theta_S \cos A_4(\cos A_1 \cos^2 A_2 + \sin^2 A_2) - \sin\theta_S \sin A_4 \sin A_2 \cos A_2(1 - \cos A_1) + \cos\theta_S(\cos A_2 \sin A_1)]} \right\}.
\tag{9}
$$

Both laser beam angles are functions of both scanner setting angles. Equations (9) have three unknown parameters: A_1, A_2, and A_3 (rad). To derive these equations, we assumed the rotation axis of the wedge scanner (see Fig. 1) is unintentionally tipped from vertical by angle A_1 in NED azimuth direction A_2. This tipping may come from the lidar mounting in the aircraft and/or from the aircraft flight attitudes, We also assumed that when the scanner motor is electronically commanded to home position, the thickest part of the optical wedge is unintentionally offset from the NED north direction by azimuth angle A_3. We assumed the laser beam perfectly aligns with the rotation axis of the optical wedge. The correct quadrant for the angle ϕ_L

must be properly accounted for. This is accomplished in many computer codes by using the atan2 function instead of the inverse tangent function.

To determine the three unknown parameters, lidar data are taken over land with $N_{AZ,CAL}$ azimuth angles per scan pattern, and the range gates with land return signals are identified. For these range gates, we assume the land is nonmoving, and Eq. (6) becomes

$$
(\nu_R^i - \nu_L^i) = \frac{2}{\lambda_L}[\sin\theta_L^i \cos\varphi_L^i(V_{AX}^i - 0)
$$
$$
+ \sin\theta_L^i \sin\varphi_L^i(V_{AY}^i - 0)
$$
$$
+ \cos\theta_L^i(V_{AZ}^i - 0)].
\tag{10}
$$

The "wind" velocity components for the ground returns have been zeroed. The aircraft velocity components may differ between different lidar scanner azimuth angle measurements. We assume they are constant during shot accumulation at one azimuth angle. The number of unknown parameters of the functional equation—in our case, 3—is the minimum value for $N_{AZ,CAL}$. The $N_{AZ,CAL}$ copies of Eq. (10), one for each value of the lidar scanner azimuth angle, are simultaneously solved to find the three unknown parameter values. These parameter values are later used when solving for the three unknown wind components. As a minimum, the parameter values should be determined following each integration of the Doppler lidar hardware into the aircraft. It would be better to determine them more often in case wind turbulence or landing bumps change the functional equation. As an example, one determination of our parameter values yielded $A_1 = -2.37 \times 10^{-5}$ rad, $A_2 = -3.79 \times 10^{-5}$ rad, and $A_3 = 0.0186$ rad (-4.9 and -7.8 arc s, and $1.1°$, respectively).

f. Solving for the unknown wind components

A copy of Eq. (6) is created for every azimuth angle to be used in solving for the unknown wind components. The functional equation is used with the appropriate parameter values discussed in the previous section. The set of Eqs. (6) is solved simultaneously for the three wind components, or, in the case of using two azimuth angles, for the two horizontal wind components.

g. Pulsed coherent lidar power carrier-to-noise ratio equation

We define the power (P) carrier-to-noise ratio (CNR_P) to be the ratio of the ensemble-mean desired signal power to the ensemble-mean undesired—hence, noise, power—and the power signal-to-noise ratio (SNR_P) as the ratio of the ensemble-mean desired signal power to the ensemble standard deviation of the desired signal power. (Some publications refer to CNR_P as SNR_P, and some publications define SNR_P as the square of CNR_P.) Since the backscattered light is from many randomly oriented aerosol particles that are randomly distributed over the illuminated volume, the received signal is a random process. Coherent detection lidars are designed so that the postdetection noise is dominated by the vacuum quantum fluctuations (numerically equal to the local-oscillator-induced shot noise model; Shapiro and Wagner 1984). Since the dominating noise is added during the optical detection process, adding another random process, there is no need to track predetection optical CNR_P—only the postdetection electrical CNR_P. The pulsed, coherent-detection lidar CNR_P equation can be written in many forms representing the trade-offs between the desire to provide physical intuition versus the desire to include as many lidar, target, and environment variations as possible. We refer the reader to any number of excellent sources, such as Gagliardi and Karp (1976, chapter 6), Kingston (1978, chapter 3), Rye (1979), Frehlich and Kavaya (1991), and Henderson et al. (2005).

For example, Eq. (7.40) in Henderson et al. (2005) is

$$CNR_P(t) = \left[\frac{P_{ST}(t)\eta_{OR}\eta_{BSR}}{h\nu B} \frac{P_N}{(P_N + P_{EN})} \right] \times \frac{\left| \iint [\eta_{QE}(x,y)\tilde{u}_{LOD}(x,y)]^* \tilde{u}_{SD}(x,y,t)\, dx\, dy \right|^2}{\left[\iint \eta_{QE}(x,y)|\tilde{u}_{LOD}(x,y)|^2\, dx\, dy \right]\left[\iint |\tilde{u}_{SD}(x,y,t)|^2\, dx\, dy \right]}. \quad (11)$$

In Eq. (11) all the quantities are ensemble averages, the superscript asterisk (*) refers to the complex conjugate of a complex number, t (s) is the time, x and y (m) are the coordinate axes perpendicular to the optical beam direction z, $P_{ST}(t)$ (W) is the desired backscattered signal optical power collected by the telescope (ST), η_{OR} is the optical receive (OR) path intensity efficiency (0–1), η_{BSR} is the beam splitter receive (BSR) path intensity efficiency (0–1), $h = 6.626 \times 10^{-34}$ (J s) is Planck's constant, B (Hz) is the receiver bandwidth, P_N (W) is the noise (N) power due to "shot noise," P_{EN} (W) is the excess noise (EN) power in addition to shot noise, $\eta_{QE}(x, y)$ (photoelectrons–photon, effectively dimensionless, and 0–1) is the optical detector's quantum efficiency (QE), $\tilde{u}$ is the complex analytic signal representation of a real-valued optical field u, $\tilde{u}_{SD}(x, y, t)(V\,m^{-1})$ is the received signal complex optical field at the detector plane (SD), and $\tilde{u}_{LOD}(V\,m^{-1})$ is the local oscillator (LO) complex optical field at the detector plane (LOD). Equation (11) assumes the LO power is constant and is large enough that shot noise dominates other light-caused noise, that total noise is white over the bandwidth, and that any quantum efficiency dependence on the intermediate frequency (IF) signal can be neglected. The denominator term $\iint |\tilde{u}_{SD}(x,y,t)|^2\, dx\, dy(V^2)$ equals the signal optical power at the detector plane, P_{SD} (W) times $2/(c\varepsilon_0)$ ($V^2/W = \Omega$), where ε_0 is the vacuum permittivity (F m^{-1}).

We may reorganize Eq. (11) to be

$$\mathrm{CNR}_P(t) = \frac{P_{\mathrm{ST}}(t)\eta_{\mathrm{OR}}\eta_{\mathrm{BSR}}}{h\nu B}\frac{P_N}{(P_N+P_{\mathrm{EN}})} \times \frac{\left|\displaystyle\iint [\eta_{\mathrm{QE}}(x,y)\tilde{u}_{\mathrm{LOD}}(x,y)]^*\tilde{u}_{\mathrm{SD}}(x,y,t)\,dx\,dy\right|^2}{\left[\displaystyle\iint |\eta_{\mathrm{QE}}(x,y)\tilde{u}_{\mathrm{LOD}}(x,y)|^2\,dx\,dy\right]\left[\displaystyle\iint |\tilde{u}_{\mathrm{SD}}(x,y,t)|^2\,dx\,dy\right]}$$

$$\times \frac{\left[\displaystyle\iint |\eta_{\mathrm{QE}}(x,y)\tilde{u}_{\mathrm{LOD}}(x,y)|^2\,dx\,dy\right]}{\left[\displaystyle\iint \eta_{\mathrm{QE}}(x,y)|\tilde{u}_{\mathrm{LOD}}(x,y)|^2\,dx\,dy\right]}. \tag{12}$$

In Eq. (12), we have divided the integral term into an equivalent product of two integral terms. Equation (12) now closely matches Eq. (3.3b) in Kingston (1978, chapter 3), who identified the first integral term as the mixing efficiency (now usually referred to as the heterodyne efficiency because of the presence of the detector quantum efficiency spatial profile), and the second integral term as the effective detector quantum efficiency.

The second integral term, the effective detector quantum efficiency $\eta_{\mathrm{QE}}^{\mathrm{EFF}}$, does not involve the signal optical field. The numerator uses the quantum-efficiency-weighted (QEW) LO optical field in the detector plane, $\tilde{u}_{\mathrm{LOD}}^{\mathrm{QEW}}$, to calculate the area-integrated irradiance yielding the optical power $P_{\mathrm{LOD}}^{\mathrm{QEWFIELD}}$ times $2/(c\varepsilon_0)$. It is this field that produces the intuitive and useful, but only conceptual, time-reversed back-propagated LO (BPLO) outside the lidar system. The denominator uses the quantum-efficiency-weighted LO irradiance in the detector plane and area averaging to calculate the ensemble-averaged power $P_{\mathrm{LOD}}^{\mathrm{QEWIRRADIANCE}}$ times $2/(c\varepsilon_0)$. It is this weighted irradiance that produces the detection shot noise, the dominating noise source. The value of $\eta_{\mathrm{QE}}^{\mathrm{EFF}}$ does not change if $\tilde{u}_{\mathrm{LOD}}$ is multiplied by a constant, and so it is independent of the LO intensity. If $\eta_{\mathrm{QE}}(x, y) = \eta_{\mathrm{QE,CONSTANT}}$, then $\eta_{\mathrm{QE}}^{\mathrm{EFF}} \rightarrow \eta_{\mathrm{QE,CONSTANT}}$.

The numerator of the first integral term, which is the heterodyne efficiency η_H, also uses the quantum-efficiency-weighted LO optical field in the detector plane $\tilde{u}_{\mathrm{LOD}}^{\mathrm{QEW}}$. It then calculates the magnitude squared of the area-integrated product of this weighted field with the received signal optical field in the detector plane. This quantity is proportional to the detector output electrical power at the intermediate frequency. The denominator normalizes the numerator by $P_{\mathrm{LOD}}^{\mathrm{QEWFIELD}}$ times $2/(c\varepsilon_0)$, and by the ensemble-averaged optical power of the signal field in the detector plane $P_{\mathrm{SD}}(t)$ times $2/(c\varepsilon_0)$. If $\eta_{\mathrm{QE}}(x, y)\tilde{u}_{\mathrm{LOD}}(x, y) = K\tilde{u}_{\mathrm{SD}}(x, y, t)$, with K a constant, then the heterodyne efficiency $\eta_H = 1$. The heterodyne efficiency does not change if $\tilde{u}_{\mathrm{SD}}$ or $\tilde{u}_{\mathrm{LOD}}$ or both are multiplied by constants, and so it is independent of the signal and LO powers. If $\eta_{\mathrm{QE}}(x, y) = \eta_{\mathrm{QE,CONSTANT}}$, then the heterodyne efficiency becomes independent of the constant quantum efficiency and $\mathrm{CNR}_P(t) \propto P_{\mathrm{ST}}(t)\eta_{\mathrm{QE,CONSTANT}}$.

h. Can airplane rotations cause significant reduction in CNR_P?

The coherent detection process requires that the ensemble-averaged return signal optical field be matched to the LO optical field in wavelength, direction, transverse size, curvature, and polarization. This leads to the question of whether CNR_P can be significantly reduced by aircraft rotations between the laser pulse emission and the detection of the backscattered light, leading to a direction difference. The sensitivity of coherent lidar CNR_P to direction difference has been published (Frehlich 1994). For GRIP flights, our maximum signal range was 16 270 m. This corresponds to a round-trip time of light of 108.5 μs. Using the DAWN laser wavelength and receiver mirror diameter, a 3-dB loss of CNR_P is caused by a direction difference of 10.3 μrad. The airplane rotation rate that would create this direction difference for the maximum range signal is 5.4° s^{-1}. Normal-level flight aircraft rotation rates are much below this amount. However, during aircraft turns, a reduction of CNR_P is expected.

i. Two figures of merit for pulsed, coherent-detection wind lidar

In addition to random velocity error σ_V (m s^{-1}) near the true velocity, there is a second and more important figure of merit (FOM) for pulsed, coherent lidar measurement of wind. This second FOM is the probability P_G that the velocity estimate is obeying the error statistics and is near to the true value—that is, it is "good" (Frehlich and Yadlowsky 1994). When one is finding the frequency of the signal peak in the frequency domain, it is easy to visualize that occasionally one or more noise peaks will be higher than the signal peak. In this case the frequency of the selected highest noise peak has no relationship to the true wind value, and we say that the velocity estimate is "bad." Bad estimates are uniformly distributed across the detection bandwidth.

As postdetection CNR_P decreases, the random velocity error of the good wind estimates increases, typically
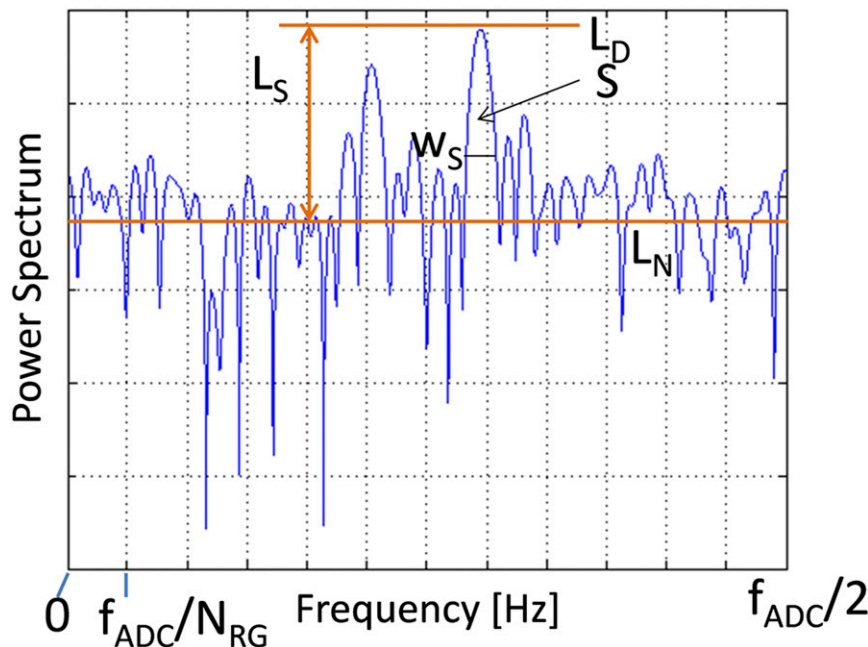
FIG. 3. Depiction of an ensemble-averaged, single-RG, shot-averaged periodogram.

going from 20% to about 90% of the backscattered signal spectrum width as CNR_P decreases by several orders of magnitude (Frehlich et al. 1997). In most cases, this remains a low velocity error measurement. However, the more dramatic effect is the simultaneous transition of P_G from 100% to a very small number. The change of P_G from 99% to 50% can occur with only a factor of 4 drop in CNR_P. The location of the P_G "cliff" compared to the changing value of σ_V depends on the shot accumulation number (Frehlich et al. 1997; Frehlich 2004).

The goal of the flights reported below was to measure wind profiles and not to determine the values of P_G and σ_V. However, the theory has been confirmed using ground-based measurements with a different lidar system (Frehlich et al. 1997).

j. Frequency domain signal processing

The coherent Doppler lidar system is designed to measure the change in light frequency between the transmitted laser pulse and the backscattered (received) light (see Figs. 1 and 2). These frequency differences are then used in Eqs. (6) and (10). The received signal is digitized and processed in the frequency domain with a computer as discussed in section 2a. For the wind measurement results presented below, the periodogram peak finding approach to frequency estimation was employed. A discrete Fourier transform (DFT) is performed by a computer on each range gate's set of N_{RG} samples. A periodogram is then calculated by taking the square of the magnitude of the complex DFT and then dividing by $N_{RG} \times T_{ADC}$, the time

length of the range gate. This is an estimate of the signal's ensemble-averaged power spectrum. [A general signal's $x(t)$ "statistical power" is considered to be $|x(t)|^2$(W), so the units of $x(t)$ are $\sqrt{W}$ and the units of the DFT of $x(t)$ are $\sqrt{W}$s. The periodogram–power spectrum then has units $W\,s^2\,s^{-1} = W\,s = W\,Hz^{-1} = J$, so areas under the periodogram have units $J\,Hz = W$].

We accumulate N_L laser shots at each laser beam direction. This shot accumulation permits wind measurements to have a higher success rate in lower concentrations of aerosols. We could also accomplish this sensitivity increase by accumulating adjacent range gates, but this would degrade the range resolution. The N_L periodograms for a specific LOS direction are registered to each other along the frequency axis by using the monitor detector in Fig. 1 to label each laser shot with the frequency difference between the injection and pulsed lasers, the pulsed laser's frequency jitter. The sum of the frequency-registered periodograms divided by N_L is a shot-averaged periodogram. The standard deviation of the averaged periodogram estimate at each frequency is approximately equal to the true power spectrum value at that frequency divided by the square root of N_L. The DAWN receiver generates real values for the ADC, so the negative frequency values of the DFT output simply repeat the positive frequency values. The negative frequency values contribute no additional information and we ignore them here. Figure 3 depicts the ensemble-averaged, single-range-gate, shot-averaged, positive frequency portion of a periodogram.

The positive portion of the DFT–periodogram output shown in Fig. 3 has values every $\Delta f_{\mathrm{DFT}} = f_{\mathrm{ADC}}/N_{\mathrm{RG}} = (500 \text{ Msample s}^{-1})/(512 \text{ samples}) = 0.977 \text{ MHz}$, going from direct current (dc) to $f_{\mathrm{MAX}} = f_{\mathrm{ADC}}/2 = 250 \text{ MHz}$. There are $N_{\mathrm{RG}}/2 = 256$ frequency intervals and $N_{\mathrm{RG}}/2 + 1 = 257$ frequency values. The periodogram ensemble-averaged noise level is L_N (W Hz^{-1}), the noise plus signal level is L_D, and the level of the signal is $L_S = L_D - L_N$. Assuming detector bias and amplification electronics are linear, the area under the signal peak but above the mean noise level is proportional to the signal power S (W). The signal peak's width w_S (Hz) may be smaller or larger than Δf_{DFT}. It is caused by factors such as the laser pulse duration, the range gate length combined with the atmospheric wind shear and wind turbulence, laser-pointing jitter during shot accumulation, and error in registering the periodograms in frequency. It is this latter contribution that leads us to zero pad our 512 sample range gates out to 2048 samples, which provides a frequency spacing of 0.244 MHz for better periodogram frequency registration.

For simplicity, we now assume that $w_S = \Delta f_{\mathrm{DFT}}$ in the following, so that $S = L_S \Delta f_{\mathrm{DFT}}$. The wideband (WB) noise is the entire area under the L_N line, namely, $N_{\mathrm{WB}} = L_N f_{\mathrm{ADC}}/2$ (W). The wideband $\mathrm{CNR}_P = \mathrm{CNR}_{P,\mathrm{WB}} = S/N_{\mathrm{WB}} = (L_S \Delta f_{\mathrm{DFT}})/(L_N f_{\mathrm{ADC}}/2) = (L_S/L_N)(2/N_{\mathrm{RG}})$. The narrowband (NB), "matched filter" noise is the area under the L_N line and under the signal, $N_{\mathrm{NB}} = L_N f_{\mathrm{ADC}}/N_{\mathrm{RG}}$. The narrowband $\mathrm{CNR}_P = \mathrm{CNR}_{P,\mathrm{NB}} = S/N_{\mathrm{NB}} = (L_S \Delta f_{\mathrm{DFT}})/(L_N f_{\mathrm{ADC}}/N_{\mathrm{RG}}] = L_S/L_N = \Phi$. Referring to Fig. 3, the narrowband result is a better figure of merit for the ability to find the signal peak in the frequency domain. The ratio of the two is $\mathrm{CNR}_{P,\mathrm{NB}}/\mathrm{CNR}_{P,\mathrm{WB}} = N_{\mathrm{RG}}/2$, which is typically two orders of magnitude. The Frehlich parameter Φ was recently defined (Frehlich and Yadlowsky 1994) and was interpreted as the average number of "coherently detected" photoelectrons per observation time.

One way to make more good wind estimates for fixed CNR_P is to narrow the region of looking for the signal peak to a frequency interval f_{SB} smaller than $f_{\mathrm{ADC}}/2$. This is accomplished by using contextual information and frequency estimates from nearby range gates. This "search band" (SB) $\mathrm{CNR}_P = \mathrm{CNR}_{P,\mathrm{SB}} = (L_S f_{\mathrm{ADC}}/N_{\mathrm{RG}})/(L_N f_{\mathrm{SB}}) = (L_S/L_N)(f_{\mathrm{ADC}}/N_{\mathrm{RG}})(1/f_{\mathrm{SB}}) = \mathrm{CNR}_{P,\mathrm{WB}}[(f_{\mathrm{ADC}}/2)/f_{\mathrm{SB}}]$.

3. Lidar system hardware

The components of a pulsed, coherent-detection, wind lidar system may be grouped in several ways. The lidar system consists of lasers, optics, electronics, mechanical structure, and software. Figure 1 shows some of these

TABLE 1. Pulsed laser parameters for DC-8 flights.

Crystal	Ho:Tm:LuLiF
Wavelength λ	2.053 472 μm
Architecture	Master oscillator power amplifier
Number of amplifiers	One, single pass
Cavity	Ring, 3.1 m long
Free spectral range	96.7 MHz
Pumping source	LDA
LDA WAVELENGTH	792 nm
LDA pulse length	1 ms
Pumping geometry	Side, 120° spacing around laser rod
Injection seeding technique	Ramp and fire
LDA cooling	Conductive
Laser rod cooling	Liquid (water)
Pulse energy, U_L	250 mJ
Pulse rate, f_L	10 Hz
Pulse duration, t_L	180 ns
Pulse frequency spectrum	Approximately transform limited
Pulse spatial quality	$M^2 < 1.2$
Output polarization	Linear, parallel to bench
Faraday isolators	Free space
Design and fabrication	NASA LaRC

subsystems. The lasers for DAWN comprise a pulsed laser and a CW laser. The optics may be grouped as small versus large optics, or as transmit path, receive path, and both paths. The electronics include power supplies, control circuits, heat removal components, and data acquisition equipment. The data acquisition electronics perform the functions of acquiring, processing, displaying, and archiving the data. The term *lidar transceiver* refers to the natural subassembly of the lasers, small optical components, and the receiver that includes the optical detectors. The large optics transform the transceiver's output laser beam into a larger beam for transmitting into the atmosphere, aiming the laser beam in the desired direction and receiving the return signal.

a. Pulsed laser

The 2-μm solid-state, pulsed laser is the heart of the coherent lidar system. It is composed of lasing media, laser-pumping components, small optics to make the resonator, and electronics to provide power and to control the laser. Our pulsed laser has been developed at the NASA Langley Research Center (LaRC) over the last two decades (Jani et al. 1995, 1997; Yu et al. 1998; Walsh et al. 2004; Yu et al. 2006). During this time, both the requirements on the pulsed laser parameters and their priorities for the future space mission have changed slightly due to wisdom gained in space instrument and mission studies. Laser requirements include pulse energy, pulse rate, and pulse duration. The relative priorities that changed over time were between pulse energy, mass,

TABLE 2. Lidar system parameters.

Transmit–receive telescope category	Off axis, reflective, afocal
Telescope type	Dall–Kirkham, beam expanding
Telescope primary mirror, D_M	Concave elliptical, 15-cm diameter
Telescope secondary mirror	Convex spherical
Telescope magnification	20
Detection	Coherent (heterodyne)
Coherent detection arrangement	Dual balanced, reverse biased
Signal optical detector	InGaAs ×2, room temperature, 75-μm diameter
Signal optical detector coupling	Alternating current
Monitor optical detector	InGaAs, room temperature
Scanner type	Rotating optical wedge
Scanner motor aperture	17.5 cm
Scanner motor mechanical home function	Yes
Scanner wedge material	Single crystal silicon, $n = 3.45$
Scanner wedge diameter	15 cm
Scanner wedge angle	11.015°
Scanner wedge beam deflection θ_S	~30.12°
Lidar optics canister pressure seal window	Fused silica, 31.75-cm diameter, 2-in. thick
Aircraft pressure seal window	Fused silica, 43.2-cm diameter, 2-in. thick
Eye safety	Eye safe at any range when canister closed for flight
INS–GPS	Hard mounted to lidar system; provides 3D orientation in NED and 3D velocity in ENU

TABLE 3. Data acquisition parameters.

Receiver analog bandwidth	10–180 MHz
LOS frequency capture bandwidth	$\pm80 = 160 = 20$–180 MHz
LOS velocity capture bandwidth	$\pm82.1 = 164.3\,\mathrm{m\,s^{-1}}$
Horizontal velocity capture bandwidth	$\pm163 = 327\,\mathrm{m\,s^{-1}} = \pm366\,\mathrm{mph}$ $= \pm318\,\mathrm{kt}$
ADC sample bits	10 bits per sample
ADC sample rate, f_{ADC}	500×10^6 samples s^{-1}
ADC sample interval	2 ns, 0.299 79 m in range, 0.259 17 m in height
Total recorded samples/intervals	55 000/54 999, 16 488.3 m in range, 14 262.0 m in height
Prelaser shot sample numbers	1–512
Monitor detector sample numbers	1–1024
Number RG samples N_{RG}	512
Signal detector sample numbers	1025–55 000
Number signal samples	53 976
Start, center, and end sample number of RG n (e.g., $n = 1$)	$1025 + 512(n - 1)$; $1280.5 + 512(n - 1)$; $1536 + 512(n - 1)$; (1025/1280.5/1536)
Start, center, and end range of RG n (e.g., $n = 1$)	$[1025 + 512(n - 2)]\,0.299\,79$ m; $[1280.5 + 512(n - 2)]\,0.299\,79$ m; $[1536 + 512(n - 2)]\,0.299\,79$ m; (153.8/230.4/307.0 m)
RG length without laser pulse	153.2 m in range, 132.5 m in height
RG length including laser pulse, R_{RES}	180.2 m in range, 155.8 m in height
Number consecutive N_{RG} RG possible	$105 = 53\,760$ samples (216 samples not used)
Start, center, and end range of RG 105	16 117.1, 16 193.7, 16 270.3 m
Maximum periodogram frequency, f_{MAX}	250 MHz, ±125 MHz, $\pm128.3\,\mathrm{m\,s^{-1}}$ LOS, $\pm255.8\,\mathrm{m\,s^{-1}}$ horizontal
Periodogram frequency spacing without zero padding, Δf_{DFT}	0.976 562 5 MHz, 1.00 m s^{-1} range, 2.00 m s^{-1} horizontal
Periodogram frequency spacing after zero padding to 2048	0.244 140 6 MHz, 0.25 m s^{-1} range, 0.50 m s^{-1} horizontal
Typical RG overlap	256 samples
Number of overlapped RG	$209 = 53\,760$ samples (216 samples not used)

volume, electrical efficiency, spatial beam quality, spectral purity, shot lifetime, and component count. The LaRC laser development team used parallel development efforts, concentrating on logical subsets of the requirements, to make faster progress. In the area of pulse energy, the LaRC team increased the demonstrated energy from 20 mJ to 1.2 J (Yu et al. 2006). For the flights reported here, the laser parameters are provided in Table 1.

b. Lidar system

The entire lidar system consists of the pulsed laser, continuous-wave (CW) laser and the other subsystems named above. Measurements from the ground in a mobile trailer have been described (Koch et al. 2007, 2010, 2012). Table 2 presents additional parameters of the lidar system. The lidar scanner is a step-stare conical scanner, permitting any laser beam direction that lies on the surface of a cone extending below the airplane and having a 30.12° half angle. The telescope is off axis to prevent backscattering of a large fraction of the laser pulse into the laser or detectors. The telescope is afocal to prevent arc breakdown of the atmosphere by the laser pulse.

Table 3 presents the data acquisition parameters used in the GRIP campaign. The signal frequency is permitted to fall anywhere in the range 10–180 MHz. If the guard band from dc was smaller than 10 MHz, then the analog electronics would be more complex. The ADC sample rate must be at least twice the upper frequency, or 360 Msample s^{-1}. We used 500 Msample s^{-1} to be well above the Nyquist frequency. The DAWN wind velocity algorithm found the frequency of the peak
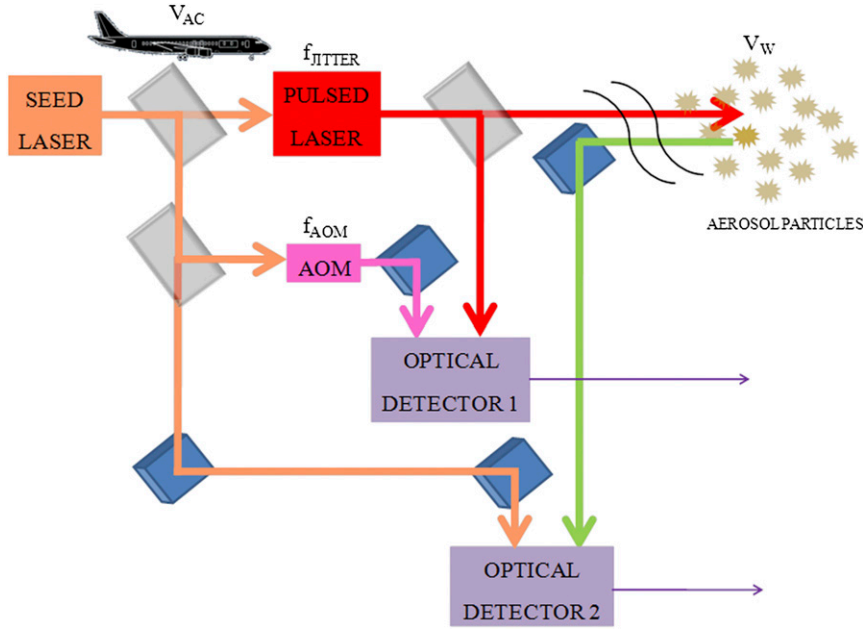
FIG. 4. Optical frequencies layout of the DAWN lidar system.

value in the shot-accumulated periodograms. Our wind measurements had line-of-sight (LOS) resolutions of 180 m and 1.0 m s^{-1}. The vertical resolution was 156 m. The horizontal wind resolution was 2.0 m s^{-1}, amplified from 1.0 m s^{-1} due to the nadir angle. Specialized signal processing algorithms to improve data processing performance have also been investigated (Beyon and Koch 2006a; Beyon et al. 2006; Beyon and Koch 2006b, 2007).

The block diagram of the optical part of the lidar system used to track frequencies is shown in Fig. 4. The stable seed laser provides injection seeding for the pulsed laser at frequency ν_{SEED}. The laser pulse frequency ν_{L} differs from the seed laser frequency by a positive or negative jitter frequency f_{JITTER}. The seed laser is also

sent directly to optical detector 2 (signal detector) and to optical detector 1 (monitor detector) after frequency upshifting by $f_{\mathrm{AOM}} = +100\,\mathrm{MHz}$. The AOM frequency shift permits the sign of the jitter frequency to be determined. The light backscattered by aerosol particles at frequency ν_R (as a function of range) is Doppler shifted by the projections onto the laser beam direction of the aircraft velocity f_{AC} and wind velocity f_W (see also Fig. 2).

Both optical detectors are used to heterodyne two sources of light. The heterodyne process causes the frequency of the detector output current to be at the absolute value of the difference frequency between the two light sources. The lhs of Eqs. (6) and (10) is found in the following way:

$$f_{\mathrm{DET1}} = |(\nu_{\mathrm{SEED}} + f_{\mathrm{AOM}}) - (\nu_{\mathrm{SEED}} + f_{\mathrm{JITTER}})| = f_{\mathrm{AOM}} - f_{\mathrm{JITTER}}$$
$$\text{assuming } f_{\mathrm{AOM}} > 0 \quad \text{and} \quad f_{\mathrm{AOM}} > |f_{\mathrm{JITTER}}|$$
$$f_{\mathrm{DET2}} = |(\nu_{\mathrm{SEED}}) - (\nu_{\mathrm{SEED}} + f_{\mathrm{JITTER}} + f_{\mathrm{AC}} + f_{\mathrm{WIND}})| = f_{\mathrm{JITTER}} + f_{\mathrm{AC}} + f_{\mathrm{WIND}}$$
$$\text{assuming } f_{\mathrm{AC}} > 0 \quad \text{and} \quad f_{\mathrm{AC}} > |f_{\mathrm{JITTER}} + f_{\mathrm{WIND}}|$$
$$\nu_R - \nu_T = f_{\mathrm{AC}} + f_{\mathrm{WIND}} = f_{\mathrm{DET1}} + f_{\mathrm{DET2}} - f_{\mathrm{AOM}}. \tag{13}$$

Equation (13) shows that the lhs of Eqs. (6) and (10) are the sum of the two detector output frequencies minus the AOM frequency, that is, minus 100 MHz. Note that f$_{\mathrm{DET1}}$ does not change with the range gate for a given laser direction and shot, and that f_{AOM} does not change with the range gate or the laser shot or the laser direction.

c. Calculation of wind velocity

For the flights reported here, a scan pattern consisted of $\theta_S \sim 30.12°$ and five directions $\phi_S = -45°, -22.5°, 0°,$ 22.5°, and 45°. We employed land backscattered signals to determine the mounting offset angles of DAWN in

TABLE 4. DAWN hardware list and DC-8 locations.

Location	Component	Subcomponent	Comments
Roof	GPS antenna		DC-8 supplied
Passenger level	Laser chillers		Three each in 19-in. rack
	Laser operator station		Electronics in 19-in. rack
	Data acquisition operator station		Electronics in 19-in. rack
Cargo level	Optics canister	Injection laser	CW
		Pulsed laser	
		Optical detector	Two each
		Telescope	
		Scanner	
		Canister window	
	Laser diode drivers		Three each
	Laser control electronics		
	Analog signal electronics		
	Scanner driver		
	Power distribution circuit		
Belly	Pressure window		
	Window port cover		Motorized; DC-8 supplied

the DC-8. Our flight paths over water limited the available land returns to islands. We used the calculated offset angles and our model for the mounting errors to find the five pairs of laser angles outside the airplane. These five directions were then modified by the three rotation angles of the airplane to obtain the laser beam directions in the NED coordinate system. Finally, the directions were converted to ENU coordinates and inserted into two or five copies of Eq. (6) for solving. We report only two azimuth angle results in this paper.

d. DC-8 accommodation

The DAWN lidar components were accommodated in both the passenger and cargo levels of the DC-8. The hardware list and the locations in the DC-8 are provided in Table 4. The pressure window at the skin of the aircraft is required. It must have a high transmission and a minimum polarization effect on the 2-μm laser beam passing through it at $\sim$30°. It must also not deform under the pressure difference to the extent of causing optical aberrations to the laser beam. The optics canister also has a pressure window that is currently used to keep dust and dirt out of the canister. In the future, it may provide a pressure seal for flight in an unpressurized compartment of a different aircraft. Having the laser chillers on the passenger level and the lasers on the cargo level required routing the cooling water between levels. This caused no problems. We began the GRIP flights with three operator stations in the passenger level. During GRIP, the ability to control the laser chillers was implemented at the laser operator station, which permitted only two operators with no requirement to move around in the airplane. The laser operator and data acquisition operator were in adjacent seats to permit both headphone and

direct communication. The DC-8 required the window port cover to be closed for takeoff and landing. The laser operator only started the laser after the port was open. The data acquisition operator occasionally stopped the software in flight, changed the number of laser shots accumulated, and restarted the software. The stopping of the software was done both to match atmospheric conditions and to learn about the DAWN performance. It was not done near a high science priority target, and only a few minutes of data were lost when it was done. The DC-8 supplied electricity, the GPS antenna, and the motorized port cover.

4. Preliminary flight results

The NASA GRIP campaign involved the flights of three aircraft in August–September 2010 (Braun et al. 2013). The DAWN lidar flew on the DC-8. Of the 25 total DC-8 flights, 15 were science flights to areas of possible hurricane development, developing storms, and mature hurricanes. Table 5 provides some statistics of DAWN's participation in GRIP.

TABLE 5. Statistics of DAWN during GRIP.

	Science flights	All flights
Number of flights	15	25
DAWN scan patterns*	11 685	13 062
DAWN laser shots	2 058 520	2 243 620
DAWN emitted photons**	5.3×10^{24}	5.8×10^{24}

* Each scan pattern yields a vertical profile of horizontal vector wind.
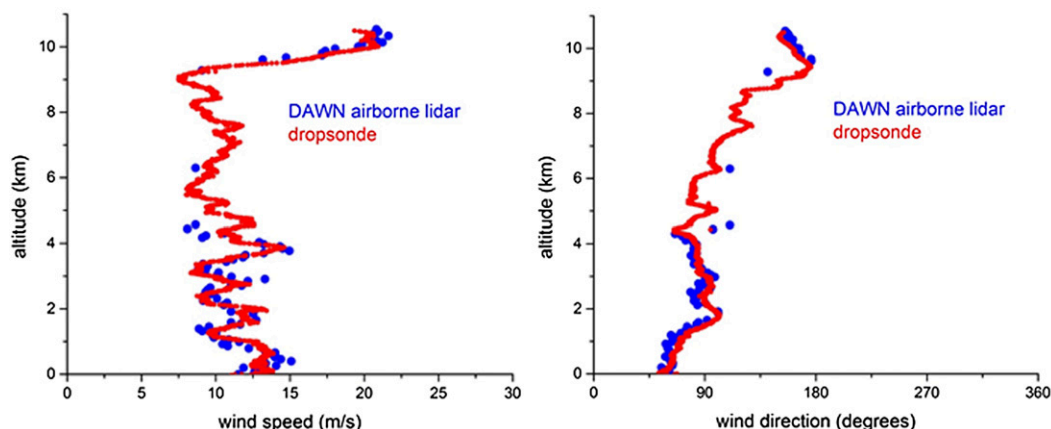
** Assuming 250-mJ laser pulses.

FIG. 5. Comparison of DAWN lidar (dots) and dropsonde (line) showing both (left) horizontal wind speed (HWS) and (right) HWD.

The DC-8 total flight time was 6712 min, and DAWN collected wind data for 5987 min or 89%. Of the 5987 DAWN data minutes, 4634 min or 95% have been processed and uploaded to the GRIP website (http://airbornescience.nsstc.nasa.gov/grip/). Each DAWN scan pattern consisted of five azimuth angles, and the number of laser shots per azimuth angle was varied between many different values from 1 to 300. The three most common values of shot accumulation were 20, 60, and 120. With a laser pulse rate of 10 Hz, these shot accumulation values have data collection times of 2, 6, and 12 s per azimuth angle, or 10, 30, and 60 s per scan pattern, respectively. The scanner azimuth change time was 2 s or so, and the computing time after each scan pattern was 2 s or so. The minimum scan pattern time was therefore 22, 42, and 72 s, respectively. With a typical DC-8 ground speed of 450 kt = 231.5 m s^{-1}(1 kt = 0.51 m s^{-1}), the minimum scan pattern horizontal resolutions were 5.1, 9.7, and 16.7 km, respectively. These are the repeat distances for the vertical profile of horizontal wind—basically the same wind product as a conventional dropsonde.

The cross-track horizontal resolution depends on the distance below the DC-8. Immediately below the DC-8, the resolution is the 15-cm telescope aperture size. (The lidar does not obtain measurements for about a 100-m distance from the airplane.) For the DC-8 flying at 10.6-km altitude, the resolution at the earth surface is about 8.7 km.

Several DAWN hardware problems were encountered during GRIP. The worst problem was a burn of the telescope secondary mirror that was not discovered until after GRIP, and after deintegration from the DC-8. We believe the burning is caused by dust settling on the mirror and being burned by the pulsed laser. The burn apparently occurred before the DC-8 flights, and it

significantly lowered our CNR$_P$ due to photon loss combined with heterodyne efficiency degradation. A second problem was the reduction of laser pulse energy, as the cold DC-8 cargo section cooled the air around our laser optics. We mitigated this in real time by adjusting laser chiller temperatures, but offsetting the mitigation was lower laser energy and some receiver misalignment caused by changing chiller temperatures. A third problem was faulting by the laser diode array power supplies. This forced a laser restart each time and a small amount of data (minutes) was lost. The vendor later fixed this problem. Finally, our initial airplane velocity removal equations used during the flights were not correct, which prevented real-time knowledge of the wind, but they did not corrupt the stored data. The total CNR$_P$ losses may have exceeded 10 dB, and our data appear as if our laser had much lower pulse energy than 250 mJ.

Preliminary data processing has used the outer two azimuth angles only from the scan patterns. Since GRIP represented the first flights of DAWN, we were eager to compare DAWN winds with dropsonde winds. Figure 5 shows an example of this intercomparison from 1 September 2010, when the DC-8 was at 10 611-m (34 813 ft) altitude. Laser shot accumulation was set to 20. The DAWN single-scan pattern shown lasted from 1720:00 to 1720:33 UTC, or 33 s. Data collection time for two azimuth angles was 4 s. The dropsonde was launched at coordinates (−75.755 711°, 29.959 888°) at 1720:15 UTC and splashed in the ocean at coordinates (−75.833 555°, 29.968 855°) at 1733:31 UTC, which is slightly over 13 min later and 7.6 km away at heading 277.6°. During the DAWN scan pattern, the DC-8 flew 7.1 km at track angle 146.1°. The dropsonde and DC-8 travel angles differed by about 132°. During the fall of the dropsonde, the DC-8 flew 172.2 km. The agreement
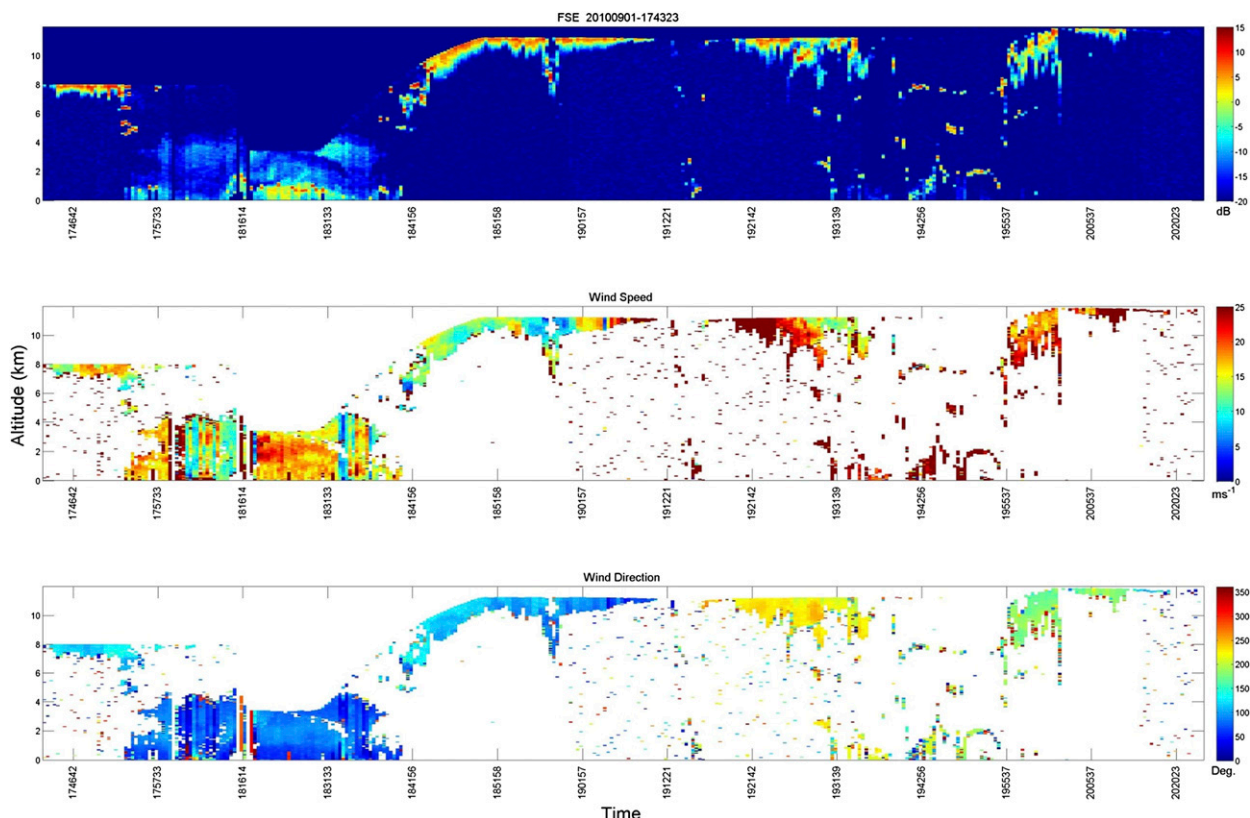
FIG. 6. Panorama display of DAWN wind data from 0 to 12 km on 1 Sep 2010 showing slightly less than 4 h of data: color-coded (top) signal energy (-20 to 15 dB in 5-dB increments), (middle) wind speed (0–25 m s^{-1} in 5 m s^{-1} increments), and (bottom) wind direction (0°–360°in 50° increments.)

between DAWN and the dropsonde is very good at altitudes just below the DC-8, and then at 0–4 km. The good low-altitude wind data eliminate the possibility of thick clouds, and we attribute the altitudes without wind measurements as due to our CNR$_P$ losses combined with the very low aerosol content ocean air. The agreement shown is not typical for our GRIP dropsonde intercomparisons due to the combination of frequent thick clouds, clean ocean air, and our CNR$_P$ losses. The areas of excellent agreement in Fig. 5 demonstrate the fundamentally correct operation of DAWN, and also indicate a stable wind field during the fall time of the dropsonde and over the ~10-km measurement separation.

Another display of wind data is the time–altitude "panorama" display shown in Fig. 6, showing slightly less than 4 h of continuous data from 1 September 2010. The laser shot accumulation was again 20. The areas with only high-altitude wind measurements most likely contained thick clouds. The areas with low-altitude or multi-altitude wind measurements most likely are free of thick clouds. It is usually the case that winds are successfully measured near the aircraft altitude. The

DC-8 flew over the eye of Hurricane Earl at approximately 1912:00 UTC. This time is about in the center of Fig. 6, where the wind direction rapidly changes from blue to yellow, or by about 180°. The top panel shows the laser beam reaching to lower altitudes within the eye, and the middle panel shows that some wind magnitudes were measured at lower altitudes within the eye.

A third type of display of wind velocities is the longitude versus latitude "top view" display, as shown in Fig. 7. The data are from 21 September 2010, and the DAWN lidar was shot accumulating 60 laser shots. The unnamed storm did not become a hurricane or even a tropical storm. Approximately 202 min of data are shown. Winds at altitudes of 2, 8, 9, 10, and 11 km are plotted. A 10 m s^{-1} wind magnitude reference vector is provided for scale. For the most part, the wind direction at different altitudes is approximately the same (easterly). The low-altitude-only winds away from the storm are indicative of the clean ocean air and our CNR$_P$ losses. As the storm is approached, the thick clouds begin and the lidar winds transition to the higher-altitude-only winds above the clouds.
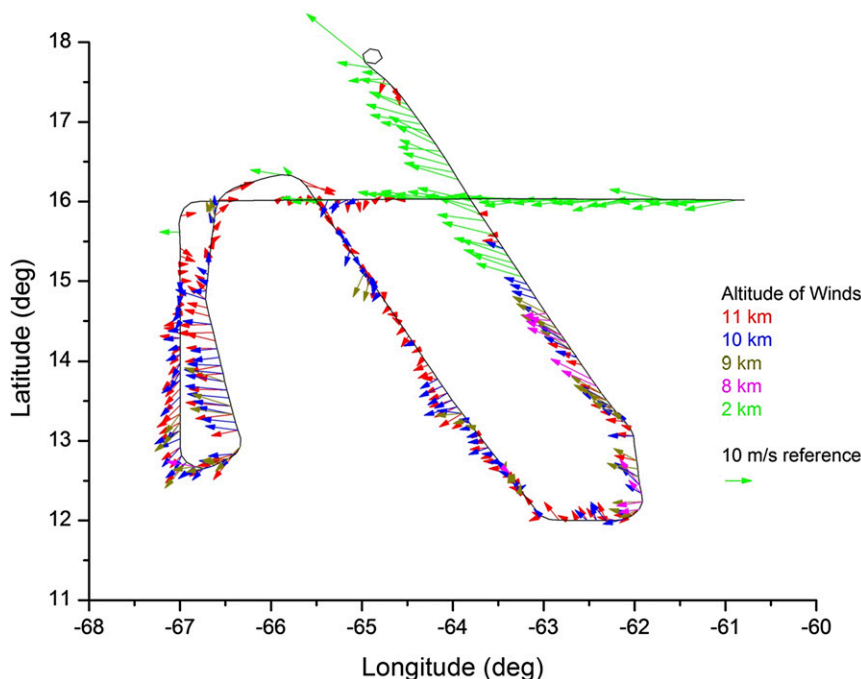
FIG. 7. Mapping of horizontal vector winds at multiple altitudes (color coded) vs longitude and latitude.

5. Conclusions

We have described results of the first flights of an airborne, 2-μm, high-energy, coherent-detection, wind-profiling lidar system developed at the NASA Langley Research Center. The combination of pulse energy, pulse rate, receiver diameter, and coherent detection have the potential to provide much improved sensitivity to aerosol backscatter levels, and therefore greater coverage of the atmosphere. The long-term motivation is to measure wind velocities from space for improved weather prediction and severe weather disaster mitigation. The interim steps of developing and testing the technology, and then the initial validation of the technology with aircraft flight, have been described. The lidar system was flown on the DC-8 during a NASA 2010 hurricane research flight campaign. Although hardware problems reduced the CNR_P, the lidar successfully measured winds throughout the campaign. Flights of the lidar on a smaller UC-12B airplane at Langley have already begun with the purpose of optimizing the lidar and developing a greater understanding of its characteristics. The Doppler lidar is generally available to collect wind data as a contribution to airborne science campaigns.

REFERENCES

Ashby, N., 2007: Relativistic effects in Earth-orbiting Doppler lidar return signals. *J. Opt. Soc. Amer.,* **24A,** 3530–3546, doi:10.1364/JOSAA.24.003530.

Baker, W. A., and Coauthors, 1995: Lidar-measured winds from space: A key component for weather and climate prediction. *Bull. Amer. Meteor. Soc.,* **76,** 869–888, doi:10.1175/1520-0477(1995)076<0869:LMWFSA>2.0.CO;2.

Beyon, J. Y., and G. J. Koch, 2006a: Resolution study of wind parameter estimates by a coherent Doppler lidar system. *Laser Radar Technology and Applications XI,* G. W. Kamerman and

M. D. Turner, Eds., International Society for Optical Engineering (SPIE Proceedings, Vol. 6214), 621403, doi:10.1117/12.663416.

——, and ——, 2006b: Wind profiling by a coherent Doppler lidar system VALIDAR with a subspace decomposition approach. *Signal and Data Processing of Small Targets 2006,* E. E. Drummond, Ed., International Society for Optical Engineering (SPIE Proceedings, Vol. 6236), 623605, doi:10.1117/12.663423.

——, and ——, 2007: Novel nonlinear adaptive Doppler-shift estimation technique for the coherent Doppler validation lidar. *Opt. Eng., 46,* 016002, doi:10.1117/1.2434768.

——, ——, and Z. Li, 2006: Noise normalization and windowing functions for VALIDAR in wind parameter estimation. *Laser Radar Technology and Applications XI,* G. W. Kamerman and M. D. Turner, Eds., International Society for Optical Engineering (SPIE Proceedings, Vol. 6214), 621404, doi:10.1117/12.663420.

Braun, S. A., and Coauthors, 2013: NASA's Genesis and Rapid Intensification Processes (GRIP) Field Experiment. *Bull. Amer. Meteor. Soc., 94,* 345–363, doi:http://dx.doi.org/10.1175/BAMS-D-11-00232.1.

Frehlich, R. G., 1994: Heterodyne efficiency for a coherent laser radar with diffuse or aerosol targets. *J. Mod. Opt., 41,* 2115–2129, doi:10.1080/09500349414551991.

——, 2004: Velocity error for coherent Doppler lidar with pulse accumulation. *J. Atmos. Oceanic Technol., 21,* 905–919, doi:10.1175/JTECH1596.

——, and M. J. Kavaya, 1991: Coherent laser radar performance for general atmospheric refractive turbulence. *Appl. Opt., 30,* 5325–5352, doi:10.1364/AO.30.005325.

——, and M. J. Yadlowsky, 1994: Performance of mean-frequency estimators for Doppler radar and lidar. *J. Atmos. Oceanic Technol., 11,* 1217–1230, doi:10.1175/1520-0426(1994)011<1217:POMFEF>2.0.CO;2.

——, S. M. Hannon, and S. W. Henderson, 1997: Coherent Doppler lidar measurements of winds in the weak signal regime. *Appl. Opt., 36,* 3491–3499, doi:10.1364/AO.36.003491.

Gagliardi, R. M., and S. Karp, Eds., 1976: *Optical Communications.* Wiley-Interscience, 432 pp.

Goldstein, H., C. P. Poole Jr., and J. L. Safko, 2001: *Classical Mechanics.* 3rd ed. Addison-Wesley, 680 pp.

Gudimetla, V. S. R., and M. J. Kavaya, 1999: Special relativity corrections for space-based lidars. *Appl. Opt., 38,* 6374–6382, doi:10.1364/AO.38.006374.

Henderson, S. W., P. Gatt, D. Rees, and R. Milton Huffaker, 2005: Wind lidar. *Laser Remote Sensing,* T. Fujii and T. Fukuchi, Eds., CRC Taylor and Francis, 469–722.

Huffaker, R. M., T. R. Lawrence, M. J. Post, J. T. Priestly, F. F. Hall Jr., R. A. Richter, and R. J. Keeler, 1984: Feasibility studies for a global wind measuring satellite system (Windsat): Analysis of simulated performance. *Appl. Opt., 23,* 2523–2536, doi:10.1364/AO.23.002523.

Jani, M. G., F. L. Naranjo, N. P. Barnes, K. E. Murray, and G. E. Lockard, 1995: Diode-pumped long-pulse-length Ho:Tm:YLiF$_4$ laser at 10 Hz. *Opt. Lett., 20,* 872–874, doi:10.1364/OL.20.000872.

——, N. Barnes, K. E. Murray, D. W. Hart, G. J. Quarles, and V. K. Castillo, 1997: Diode-pumped Ho:Tm:LuLiF$_4$ laser at room temperature. *IEEE J. Quantum Electron., 33,* 112–115, doi:10.1109/3.554905.

Kavaya, M. J., and R. T. Menzies, 1985: Lidar aerosol backscatter measurements: Systematic, modeling, and calibration error considerations. *Appl. Opt., 24,* 3444–3453, doi:10.1364/AO.24.003444.

Kingston, R. H., 1978: *Detection of Optical and Infrared Radiation.* Springer Series in Optical Sciences, Vol. 10, Springer-Verlag, 140 pp.

Koch, G. J., J. Y. Beyon, B. W. Barnes, M. Petros, J. Yu, F. Amzajerdian, M. J. Kavaya, and U. N. Singh, 2007: High-energy 2μm Doppler Lidar for wind measurements. *Opt. Eng., 46,* 116201, doi:10.1117/1.2802584.

——, and Coauthors, 2010: Field testing of a high-energy 2-μm Doppler lidar. *J. Appl. Remote Sens., 4,* 043512, doi:10.1117/1.3368726.

——, J. Y. Beyon, E. A. Modlin, P. J. Petzar, S. Woll, M. Petros, J. Yu, and M. J. Kavaya, 2012: Side-scan Doppler lidar for offshore wind energy applications. *J. Appl. Remote Sens., 6,* 063562, doi:10.1117/1.JRS.6.063562.

Menzies, R. T., and D. M. Tratt, 1997: Airborne lidar observations of tropospheric aerosols during the Global Backscatter Experiment (GLOBE) Pacific circumnavigation missions of 1989 and 1990. *J. Geophys. Res., 102,* 3701–3714, doi:10.1029/96JD03405.

NASA, 2006: Working group report. J. Neff and A. Valinia, Eds., Lidar Technologies, 171 pp. [Available online at http://esto.nasa.gov/files/LWGReport2006.pdf.]

NRC, 2007: *Earth Science and Applications from Space: National Imperatives for the Next Decade and Beyond.* The National Academies Press, 456 pp.

Rye, B. J., 1979: Antenna parameters for incoherent backscatter heterodyne lidar. *Appl. Opt., 18,* 1390–1398, doi:10.1364/AO.18.001390.

——, and R. G. Frehlich, 1992: Optimal truncation and optical efficiency of an aperture coherent lidar focused on an incoherent backscatter target. *Appl. Opt., 31,* 2891–2899, doi:10.1364/AO.31.002891.

Shapiro, J. H., and S. S. Wagner, 1984: Phase and amplitude uncertainties in heterodyne detection. *IEEE J. Quantum Electron., 20,* 803–813, doi:10.1109/JQE.1984.1072470.

Singh, U. N., S. Ismail, M. J. Kavaya, D. M. Winker, and F. Amzajerdian, 2005: Space-based lidar. *Laser Remote Sensing,* T. Fujii and T. Fukuchi, Eds., CRC Taylor & Francis, 781–881.

Taff, L. G., 1983: Relativity and radars. MIT/LL Tech. Rep. 660, AD-A133791, 22 pp.

Walsh, B., N. Barnes, M. Petros, J. Yu, and U. Singh, 2004: Spectroscopy and modeling of solid state lanthanide lasers: Application to trivalent Tm^{3+} and Ho^{3+} in YLiF$_4$ and LuLiF$_4$. *J. Appl. Phys., 95,* 3255, doi:10.1063/1.1649808.

Yu, J., U. Singh, N. Barnes, and M. Petros, 1998: 125-mJ diode-pumped injection-seeded Ho:Tm:YLF laser. *Opt. Lett., 23,* 780–782, doi:10.1364/OL.23.000780.

——, and Coauthors, 2006: 1 J/pulse *Q*-switched 2 μm solid-state laser. *Opt. Lett., 31,* 462–464, doi:10.1364/OL.31.000462.